nature energy

Article

https://doi.org/10.1038/s41560-025-01736-6

Enhanced solar water oxidation and unassisted water splitting using graphite-protected bulk heterojunction organic photoactive layers

Received: 8 December 2023

Accepted: 6 February 2025

Published online: 18 March 2025

Check for updates

Matyas Daboczi[1,2] ✉, Flurin Eisner[3,4] ✉, Joel Luke[5], Shi Wei Yuan[5], Noof Al Lawati[1], Maoqing Zhi[1,5], Mengya Yang[1], Jolanda Simone Müller[5], Katherine Stewart[5], Ji-Seon Kim[5], Jenny Nelson[5] ✉ & Salvador Eslava[1] ✉

Polymer donors and non-fullerene acceptors have played an important role as photoactive materials in the development of high-efficiency organic solar cells and have immense potential in devices for direct solar hydrogen generation. However, their use in direct solar water-splitting devices has been limited by their instability in aqueous environment and recombination losses at the interface with catalysts. Here we report anodes containing PM6:D18:L8-BO photoactive layers reaching high solar water oxidation photocurrent density over 25 mA cm^{-2} at +1.23 V versus reversible hydrogen electrode and days-long operational stability. This was achieved by integrating the organic photoactive layer with a graphite sheet functionalized with earth-abundant NiFeOOH water oxidation catalyst, which provides both water resistance and electrical connection between the catalyst and the photoactive layer without any losses. Using monolithic tandem anodes containing organic PM6:D18:L8-BO and PTQ10:GS-ISO photoactive layers, we achieve a solar-to-hydrogen efficiency of 5%. These results pave the way towards high-efficiency, stable and unassisted solar hydrogen generation by low-cost organic photoactive materials.

One of the most pressing challenges in achieving net zero is the production of inexpensive low-emission fuels[1]. Direct solar water splitting is a promising route towards off-grid, low-cost hydrogen production with a low environmental footprint[2]. In particular, photoelectrochemical (PEC) cells can offer sustainable, low-cost systems with high solar-to-hydrogen (STH) efficiency[3,4]. However, existing PEC systems have thus far failed to achieve the combination of high performance, long-term stability, low manufacturing cost and use of earth-abundant materials[5,6].

Organic semiconductors are compatible with eco-friendly and low-cost large-scale manufacturing methods[7–9] and are also promising candidates for efficiently driving PEC reactions due to their tunable optoelectronic properties[10–12]. Recently, building on high-performing donor–acceptor bulk heterojunction (BHJ) organic photovoltaic (OPV) devices, encouraging progress has been achieved on both BHJ photocathodes and photoanodes[13–18]. However, despite these demonstrations, there has been limited

[1]Department of Chemical Engineering and Centre for Processable Electronics, Imperial College London, London, UK. [2]Institute of Technical Physics and Materials Science, HUN-REN Centre for Energy Research, Budapest, Hungary. [3]Department of Materials, Imperial College London, London, UK. [4]School of Engineering and Materials Science, Queen Mary University of London, London, UK. [5]Department of Physics and Centre for Processable Electronics, Imperial College London, London, UK. ✉e-mail: m.daboczi@imperial.ac.uk; f.eisner@qmul.ac.uk; jenny.nelson@imperial.ac.uk; s.eslava@imperial.ac.uk

success in translating the high photocurrent densities (j_{ph}) achievable in BHJ OPV devices (>25 mA cm^{-2}) into PEC cells (2–15 mA cm^{-2}), especially in conjunction with operational stability on the order of days[18,19].

A major challenge to improving solar-to-fuel conversion efficiencies in organic PEC cells is minimizing electronic losses between the photo-absorbing organic semiconductor and the electrocatalyst[14,15,19]. This is particularly important for photoanodes, where the sluggish oxidation reaction kinetics can lead to rapid build-up of charges at the organic semiconductor–electrocatalyst interface that decrease efficiency and lead to degradation of the organic semiconductor[10,14]. Previous efforts to address this have included using polymer[14,16] or metal-oxide[20,21] interlayers, as well as more elaborate (and expensive) encapsulation techniques[17]. All these cited PEC devices apply a fully integrated structure, different to wired photovoltaic–electrolyser devices. These devices are commonly denoted as 'photoanodes' or 'photoelectrodes', despite the integration of further semiconductor and/or highly conductive layers on top of the photoactive material, which differentiates them from the traditional photoelectrodes comprising a direct semiconductor–electrolyte interface. To distinguish these traditional photoanodes from photovoltaics integrated into monolithic anodes using protection layers, we introduce the term integrated photovoltaic anode (IPV-anode) to refer to such integrated devices including the ones introduced in this Article (see further discussion in Supplementary Note 1).

Here, we present BHJ IPV-anodes that apply a straightforward and cost-effective approach using self-adhesive graphite sheet functionalized with an earth-abundant nickel–iron oxyhydroxide (NiFeOOH) electrocatalyst to simultaneously prevent degradation by the aqueous environment and eliminate electrical losses between the BHJ photoactive layer and the catalyst. The single-junction IPV-anodes reach a j_{ph} of over 25 mA cm^{-2} at +1.23 V versus reversible hydrogen electrode (V_{RHE}) and days-long operational stability, and monolithic organic tandem IPV-anodes achieve unassisted (that is, bias-free) solar water splitting in a two-electrode setup with 5% STH efficiency.

Fabrication of organic IPV-anodes

The schematic structure of the fabricated organic IPV-anodes and the related energy band diagrams and chemical composition of the materials used in optimized devices are shown in Fig. 1. In the optimized devices, a SnO_2 electron transport layer (ETL) and a MoO_3 hole transport layer (HTL) were used. The organic photoactive layer comprises a ternary blend of PM6 and D18 donor polymers, absorbing in the 400–700 nm wavelength range due to their relatively large optical bandgaps (1.9 and 2.1 eV, respectively), and L8-BO, a non-fullerene acceptor that absorbs photons up to 900 nm wavelength due to its narrow optical bandgap (1.45 eV). The top of the IPV-anodes consists of a 70-µm-thick graphite sheet functionalized with NiFeOOH on the front side and adhesive on the back side. This sheet is attached directly to the thin (30/10 nm) top MoO_3/gold contact of the photoactive layer and serves simultaneously as a water-resistant and electrically conductive protective layer and electrocatalyst. The graphite sheet has highly oriented layers and large porosity (10–50 µm pores, 50% porosity), providing large surface area for the electrodeposition of the NiFeOOH electrocatalyst[22].

The highest occupied molecular orbital (HOMO) and Fermi level values of the separate device layers were measured by ambient photoemission spectroscopy (Supplementary Fig. 1) and Kelvin probe (Supplementary Fig. 2), respectively. The energy levels of the lowest unoccupied molecular orbitals (LUMOs) for the organic semiconductors were calculated using the HOMO and the optical bandgap values to construct the energy band diagrams of all constituent layers of the IPV-anode (Fig. 1b). Importantly, the HOMO of both donor polymers (−5.05 eV) lie deeper than the theoretical electrochemical potential of water oxidation at pH 14 (−4.90 eV), a thermodynamic requirement for water oxidation and an advantage in achieving a low onset potential (E_{on}) for photoanodes.

Solar water oxidation performance of organic IPV-anodes

The successful electrodeposition of the NiFeOOH electrocatalyst on the graphite sheet was confirmed by a more than 500 mV cathodic shift in E_{on} for water oxidation at pH 14 (Supplementary Fig. 3). These functionalized graphite sheets were attached to the thin metal electrode of OPVs, which include various HTLs and ETLs (Supplementary Figs. 4 and 5). We found that the SnO_2 ETL and MoO_3 HTL yielded the highest j_{ph} at +1.23 V_{RHE}, plausibly due to the improved charge carrier extraction and higher photovoltage resulting in a reduced E_{on}. The increased photovoltage is also reflected in the larger change in open circuit potential (ΔOCP) of the IPV-anodes upon switching off the 1 sun illumination (Supplementary Figs. 4 and 5). The optimized 0.28 cm^2 active area IPV-anodes showed a champion j_{ph} of 26.4 mA cm^2 (average of 23.8 ± 2.1 mA cm^2) at +1.23 V_{RHE} and an E_{on} as low as +0.66 V_{RHE} (average of +0.69 ± 0.02 V_{RHE}) both under continuous and chopped 1 sun illumination, in aqueous 1 M NaOH electrolyte at pH 14 (Fig. 2a,b). E_{on} was determined conservatively by linear fitting of the photocurrent rise. The saturation of j_{ph} above +1.4 V_{RHE} was confirmed by subtracting the dark current density from the current density under 1 sun illumination (Supplementary Fig. 6).

The IPV-anodes with the functionalized graphite sheet generated stable j_{ph} above 20 mA cm^2, even when using a ultraviolet (UV) filter (Fig. 2c). This is in stark contrast with the two orders of magnitude lower j_{ph} (~0.2 mA cm^2) generated by a device lacking the graphite sheet. While devices with a thicker gold layer of 100 nm achieved an initial j_{ph} of 9.4 mA cm^2, they fully degraded within 15 min without the graphite sheet (Supplementary Fig. 7). These control measurements demonstrate the essential role of the graphite sheet in protecting the photoactive layer from degradation by the aqueous electrolyte. Similarly, devices with only the graphite sheet, but without MoO_3–Au layers showed negligible j_{ph}, highlighting the necessary role of these layers in providing effective charge extraction (Supplementary Fig. 7). The short-circuit current density (J_{sc}) of up to 26.8 mA cm^{-2} of solar cells (Supplementary Fig. 11) agrees well with the high j_{ph} measured in the graphite sheet containing IPV-anodes (26.4 mA cm^2).

Recombination losses in the organic solar cells with and without the graphite sheet were investigated by light-intensity-dependent open circuit voltage, V_{oc}, (Fig. 2d) and J_{sc} (Supplementary Fig. 8) measurements. Deposition of the graphite sheet had minimal effect on the light-intensity dependence of solar cells, which suggests the elimination of most electrical losses between the top electrode of the organic BHJ solar cell and the catalyst-functionalized graphite sheet. This was confirmed by the almost identical electroluminescence, external quantum efficiency spectra (Supplementary Fig. 9), current–voltage curves (Supplementary Fig. 10) and voltage losses (Supplementary Table 1). These results show that the predeposited adhesive layer at the back of the graphite sheet is thin and/or discontinuous enough to ensure direct electrical contact between the rough graphite sheet and the Au top electrode; therefore, no conductive fillers are needed in the adhesive layer[23]. Importantly, these results demonstrate that the addition of the graphite sheet with its adhesive and NiFeOOH layers does not significantly impact charge recombination.

A necessary requirement to achieve a high j_{ph} is the preparation of uniform, pinhole-free photoactive layers with high shunt resistance (measured between the bottom indium tin oxide (ITO) and top graphite sheet electrodes in this case). We found that increasing the thickness of the photoactive layer from around 110 nm (the optimum for solar cells) to above 200 nm significantly enhanced performance by increasing shunt resistance (Supplementary Fig. 12). The relatively large standard deviation (±2.1 mA cm^{-2}) of j_{ph} measured at +1.23 V_{RHE} for seven devices from different batches (Supplementary Fig. 13) is

https://doi.org/10.1038/s41560-025-01736-6

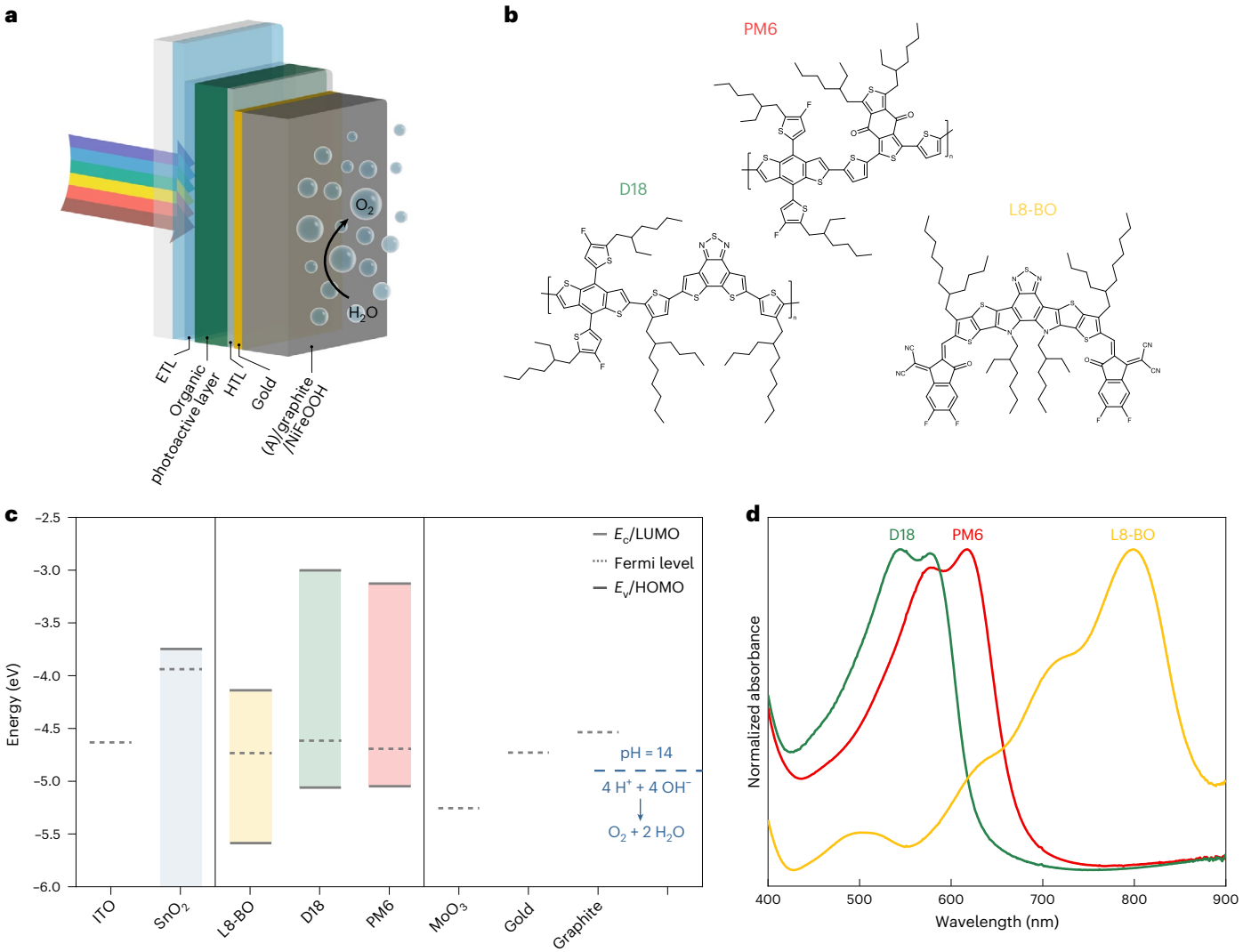

Fig. 1 | Structure, composition and energetics of the PM6:D18:L8-BO organic IPV-anodes. a, A schematic representation of the water oxidation IPV-anodes containing an organic photoactive layer and a self-adhesive (A) graphite sheet as a conductive protection layer (not to scale). The adhesive layer is not shown, as there is direct electrical contact between the gold and graphite layers. **b**, The chemical structures of PM6, D18 and L8-BO, the three photoactive materials in the ternary BHJ blend. **c**, The energy level diagrams for all the constituent layers of the organic IPV-anode. The shaded areas represent the bandgap of the semiconductors. The blue dashed line indicates the electrochemical potential of water oxidation to oxygen at pH 14. **d**, The normalized absorbance spectra of PM6, D18 and L8-BO.

potentially due to the effect of varying active layer uniformity and resistance, especially for larger (0.28 cm^2) devices. The statistical analysis of smaller area (0.05 cm^2) OPV also shows a similar trend: small variation in V_{oc} (0.89 ± 0.01 V) but larger in J_{sc} (25.1 ± 0.9 mA cm^{-2}) and fill factor (0.63 ± 0.03) (Supplementary Fig. 11), suggesting that the effect of active layer uniformity and shunt resistance is also present in the solar cells. Overall, the statistical analysis of IPV-anodes and solar cells confirm the high j_{ph} achieved close to the theoretical limit (~31 mA cm^{-2})[24]. Accordingly, the incident photon-to-current efficiency (IPCE) at +1.23 V_{RHE} of the organic IPV-anodes reached close to 90% in the 600–800 nm wavelength range, with an integrated j_{ph} of 23.5 mA cm^{-2} (Fig. 2e). The amount of generated O_2 gas during continuous operation on this IPV-anode was measured, yielding a high Faradaic efficiency of 97% (Fig. 2f).

Polymer:polymer IPV-anodes were also fabricated with an organic photoactive layer comprising the polymers PM6 and PY-IT. These polymer:polymer IPV-anodes also achieved a high average j_{ph} of 23.3 mA cm^{-2} at +1.23 V_{RHE} and an E_{on} of +0.63 V_{RHE}, which is a 60 mV improvement compared with the ternary PM6:D18:L8-BO devices (Supplementary Fig. 14). The lower E_{on} is in accordance with the higher photovoltage indicated by ΔOCP measurements (Supplementary Fig. 14), which results from reduced non-radiative voltage losses in these polymer:polymer solar cells[25].

Differences between PEC and solar cell operation

To gain insight into the operation and losses of the organic IPV-anodes, light-intensity-dependent measurements were performed on the devices as IPV-anodes in PEC cells and as solar cells (Fig. 3). The j_{ph} of organic IPV-anodes at +1.23 V_{RHE} and the J_{sc} of organic solar cells both show a linear relationship on a log–log scale against the light intensity. This relationship remains true for the full range of light intensities for the solar cells; however, the j_{ph} of the IPV-anodes fall below the power-law fit at light intensities lower than 30 mW cm^{-2} (Fig. 3b,e). This implies increased recombination in the IPV-anodes at lower photogenerated charge carrier densities, possibly originating from the electrocatalyst–electrolyte interface. A similar trend is observed in the IPV-anode photovoltage and solar cell V_{oc} with light intensity (Fig. 3c,f). The photovoltage of the organic IPV-anode was

https://doi.org/10.1038/s41560-025-01736-6

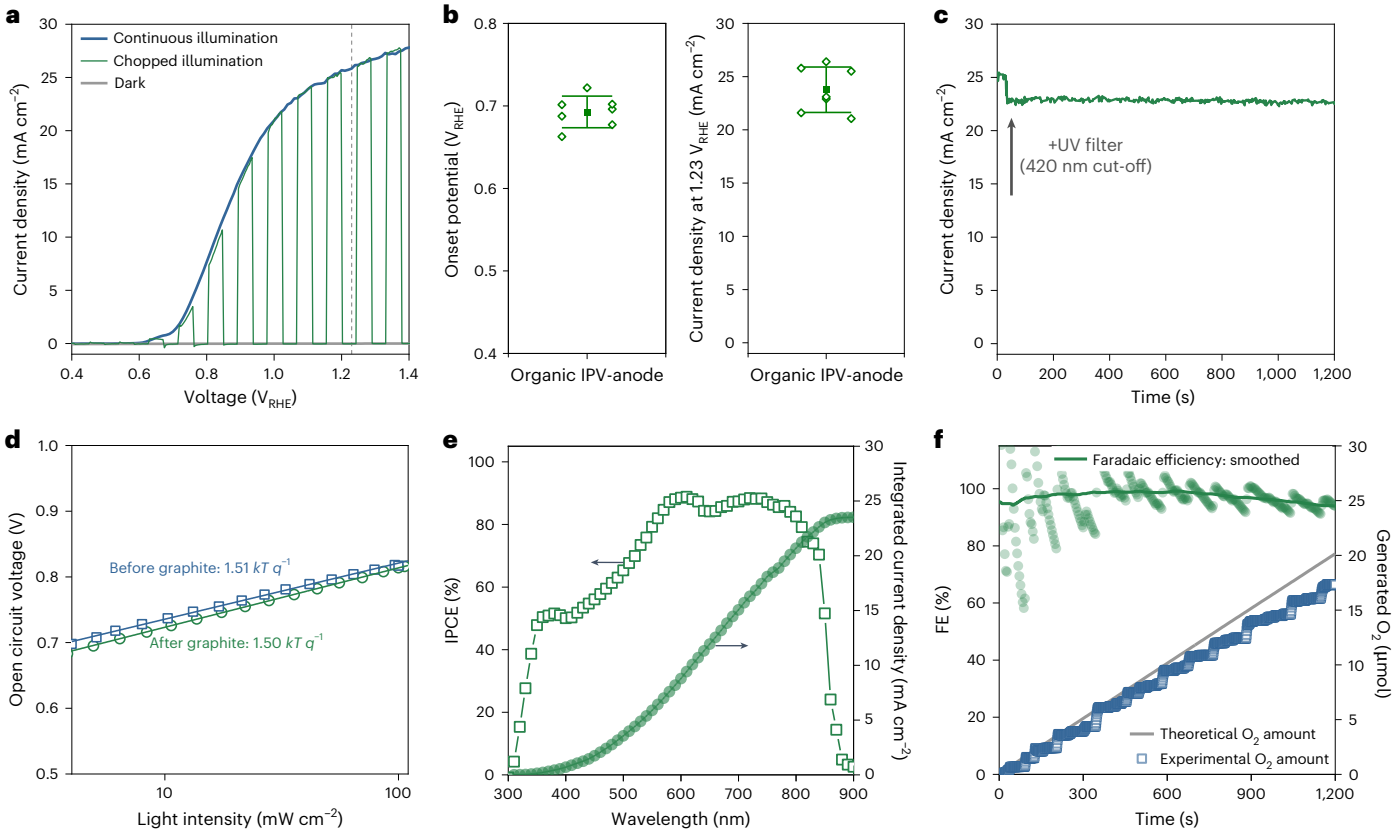

Fig. 2 | Performance of PM6:D18:L8-BO organic IPV-anodes with 0.28 cm² active area measured in a PEC cell. a, Current density–voltage scans in the dark, under one sun continuous and chopped illumination for a high-performing PM6:D18:L8-BO IPV-anode. The scan rates were 20 mV s^{-1} for chopped illumination and 50 mV s^{-1} for the rest. The vertical dashed line at +1.23 V_{RHE} indicates the standard oxidation potential of water to oxygen. **b**, The distribution of the onset potentials and photocurrent densities at +1.23 V_{RHE} extracted from the current–voltage scans of seven organic IPV-anodes from different batches. The open diamond symbols show the values measured for the individual devices (lateral displacement is only for clarity), the solid squares are the mean values and the whiskers represent one standard deviation. **c**, The stabilized photocurrent density of a representative PM6:D18:L8-BO IPV-anode under 1 sun illumination without (0–30 s) and with (30–1,200 s) a 420 nm cut-off UV filter. **d**, The light-intensity-dependent open circuit voltage of the organic IPV-anode before and after deposition of the top graphite sheet. The open symbols represent the measured data points, while the solid lines show fitting by least squares regression. **e**, The IPCE spectra and integrated photocurrent density at +1.23 V_{RHE} of a representative organic IPV-anode. **f**, The Faradaic efficiency of an organic IPV-anode calculated from the measured amount of generated O_2 compared with the theoretical amount of O_2 based on the recorded photocurrent. The green solid circles represent the Faradaic efficiency values, while the green solid line shows the same data smoothed with percentile filter method using points of window of 600. The measurements were performed in an aqueous 1 M NaOH electrolyte in a PEC cell.

estimated by the onset potential shift under illumination compared with the water oxidation onset potential measured in dark for the NiFeOOH-functionalized graphite sheet. The onset potential values were extracted from the first-order derivative at 3 mA cm^{-2} V^{-1} (Supplementary Fig. 15)[26]. The light-intensity dependence of V_{oc} again shows a linear relationship on a semi-log scale for the organic solar cells with a slope of 1.50 $kT\,q^{-1}$ (meaning a light ideality factor of 1.50), where kT is the thermal energy and q is the elementary charge. However, the relationship of the IPV-anode photovoltage and the light intensity follows the power-law fit only at high light intensities (>30 mW cm^{-2}) with a slope of 1.54 $kT\,q{-}1$, which significantly increases at lower light intensities (up to 2.81 $kT\,q^{-1}$). This reveals only slight difference under 1 sun illumination but increased recombination at low light intensities (<30 mW cm^{-2}) in the organic IPV-anodes compared with the solar cells, however[27,28].

Considering the same composition and structure of the solar cell and IPV-anode devices, the distinctly different light-intensity dependence points to the IPV-anode–electrolyte interface as the origin of increased recombination. In a solar cell applying a contact layer with deep enough work function, there is straightforward extraction of photogenerated holes even at low charge carrier densities. However, IPV-anode charge extraction (that is, injection into the electrolyte) happens only via multiple reaction steps; for example, water oxidation and oxygen evolution steps involve four holes per O_2 molecule, which all occur in the presented IPV-anodes as confirmed by the high Faradaic efficiency (Fig. 2f). The kinetics as well as the oxidation potential of the reaction with respect to the energetics of the IPV-anode could influence the charge extraction and recombination rate at the IPV-anode–electrolyte interface, which we investigated by performing light-intensity-dependent ΔOCP measurements that allow the minimization of the kinetic influence[29] by adding a Na_2SO_3 hole scavenger to the alkaline electrolyte and by reducing the pH of the electrolyte from 14 to 10 (Supplementary Figs. 16–21). The results reveal that the value of ΔOCP relates closely to the photovoltage generated by the IPV-anode and that it is not influenced by the mixed potential measured at OCP in dark[30]. More importantly, the results confirm that the charge injection at the IPV-anode–electrolyte interface is limited during oxygen evolution reaction due to insufficient energetic driving force at low light intensities (see Supplementary Note 2 for a detailed discussion). Application of deeper energy level photoactive materials (especially deeper HOMO of the donor) in organic IPV-anodes could potentially reduce such recombination at lower light intensities.

https://doi.org/10.1038/s41560-025-01736-6

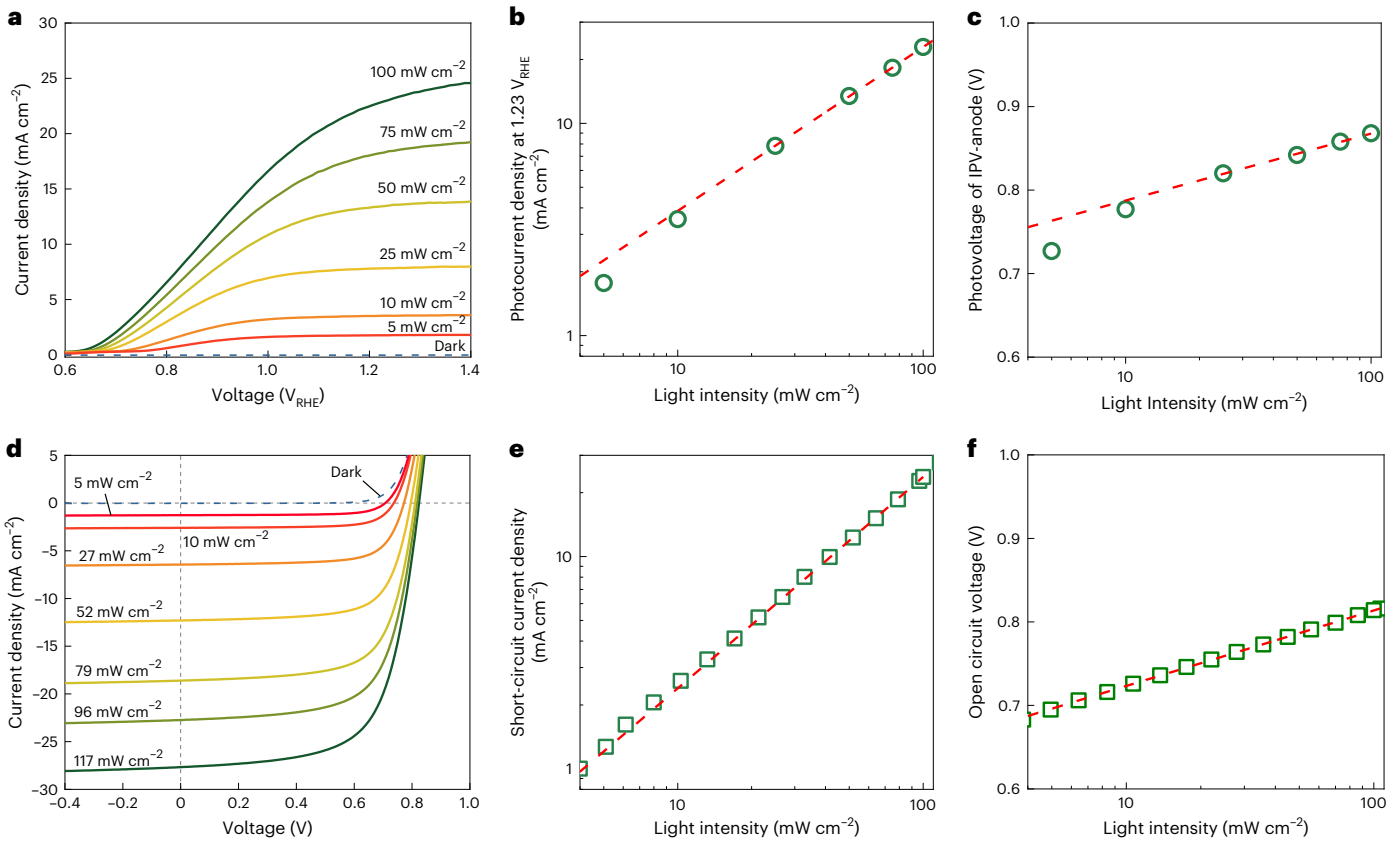

Fig. 3 | Light-intensity dependence of PM6:D18:L8-BO organic IPV-anodes and solar cells. a, The current density–voltage scans of the PM6:D18:L8-BO IPV-anode at different light intensities measured in aqueous 1 M NaOH electrolyte at a 50 mV s^{-1} scan rate. **b**, The photocurrent density at +1.23 V_{RHE} extracted from the current–voltage curves. **c**, The photovoltage of organic IPV-anode calculated from the onset potential shift under illumination by different light intensities compared with the dark current–voltage scan of the reference catalytic sheet. **d**, The current density–voltage scans of PM6:D18:L8-BO organic solar cells at different light intensities and a 40 mV s^{-1} scan rate. **e**,**f**, The light-intensity dependence of short-circuit current density (**e**) and open circuit voltage (**f**) of the organic solar cells. The open symbols represent the measured data points, while the solid lines show fitting by least squares regression.

Stability of organic IPV-anodes

The developed graphite-protected PM6:D18:L8-BO IPV-anodes were tested in lab ambient conditions and under different operational conditions to understand their degradation mechanisms and improve their stability. The high initial j_{ph} at +1.23 V_{RHE} applied potential was found to decay linearly after the first 0.5 h at a rate of 1.5 mA cm^{-2} h^{-1} under 1 sun illumination, which slowed down to 0.5 mA cm^{-2} h^{-1} when applying a UV filter (Fig. 4a). This detrimental UV light-driven degradation has been widely reported in OPV devices and assigned to degradation of the BHJ photoactive layer triggered by adjacent metal-oxide transport layers. This light-induced degradation is slower but still present with SnO_2 ETL[31–33]. Measurement of the IPV-anodes as solar cells for 8 h under continuous illumination (without a UV filter) showed a roughly 15% decay of the initial photocurrent (Fig. 4b and Supplementary Fig. 22). These results suggest that a significant amount of j_{ph} decay originates from the photoinduced degradation of the organic photoactive layer and not from the graphite sheet interface or the presence of aqueous electrolyte.

Photoluminescence (PL) spectra recorded after 72 h of PEC operation within and outside the active area further confirm the degradation of the organic absorber layer (Fig. 4c). The active area is defined as the area illuminated (back side) and in contact with electrolyte (front side) during operation. In both areas, the PL emission is dominated by L8-BO (880 nm) due to effective energy transfer to the narrower bandgap component, although a small contribution from polymer emission can also be observed at 650–700 nm. The L8-BO emission peak is red shifted within the active area compared with outside, which suggests enhanced acceptor crystallinity and indicates phase separation between L8-BO acceptor and polymer donor. Such phase separation leads to less intermixed blend morphology, which will reduce charge generation, possibly leading to the observed loss of photocurrent. The fresh IPV-anodes before operation show no PL peak shift between the different areas of the device, confirming the PL changes observed are due to prolonged photoexcitation of the device (Supplementary Fig. 23)[34,35].

The photodegradation of PM6 and D18 as well as polymer:polymer films was also investigated, as they are known to degrade rapidly in air under illumination (Supplementary Figs. 24–26)[36]. Based on the Raman spectra of degraded devices and UV–visible light spectra of ex situ degraded photoactive layers, we conclude that the morphological instability of these organic blend IPV-anodes is the main mechanism affecting operational stability in PEC cells (see Supplementary Note 3 for a detailed discussion).

The loss of NiFeOOH catalyst during continuous operation from the surface of the graphite sheet is evident from the accelerated photocurrent decay after 16–20 h (Supplementary Fig. 27). This is confirmed by X-ray photoelectron spectroscopy (XPS) measurements, by the recovery of photocurrent when replacing the NiFeOOH-functionalized graphite sheet and by the presence of visible graphite particles in the electrolyte (Supplementary Figs. 28–32 and Supplementary Note 4). We tested a thicker, porous graphite sheet (150 µm thick) with a thicker layer of NiFeOOH, which helped minimizing losses due to catalyst degradation (Supplementary Fig. 33). Based on these results, we also fabricated PM6:D18:L8-BO IPV-anodes with a thicker NiFeOOH catalyst

https://doi.org/10.1038/s41560-025-01736-6

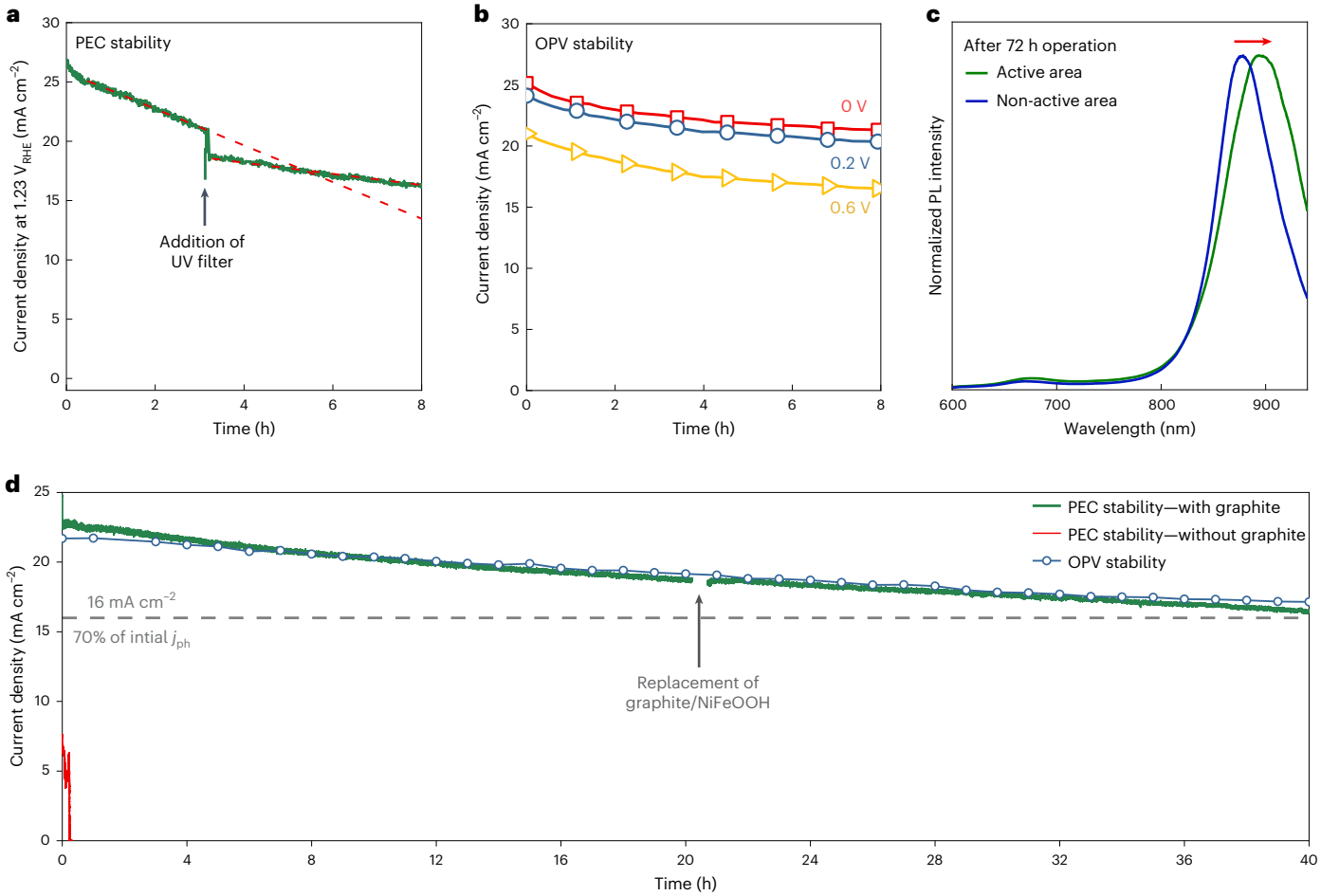

Fig. 4 | Operational stability of PM6:D18:L8-BO organic IPV-anodes in PEC cells and as solar cells at ambient conditions. a, A comparison of operational photocurrent stability of the organic IPV-anode at +1.23 V_{RHE} under 1 sun illumination without and with a 420 nm cut-off UV filter measured in a PEC cell. The red dashed lines show the linear fits by least squares regression to the two phases of photocurrent decay. **b**, The photocurrent stability of the organic IPV-anode measured as solar cell (OPV stability) under continuous illumination without UV filter. **c**, The normalized PL spectra of the photoactive layer of a full organic IPV-anode after 72 h of continuous operation at +1.23 V_{RHE} in a PEC cell. The red arrow indicates the shift in peak position between the PL spectra recorded within the 0.28 cm^2 active area (illuminated under operation) and outside of the active area (not illuminated). **d**, The operational photocurrent stability of an OPV at 0.2 V and an organic IPV-anode for 40 h under 1 sun illumination at +1.23 V_{RHE} with the use of a 420 nm cut-off UV filter with and without applying graphite protection. The dashed horizontal line indicates 70% of the initial j_{ph} of the organic IPV-anode. After 22 h of operation, the NiFeOOH-functionalized 150-µm-thick graphite sheet was replaced with a fresh one. The PEC cell electrolyte was aqueous 1 M NaOH.

layer and measured its long-term stability, as shown in Fig. 4d. These IPV-anodes showed an unprecedented 40 h long operational water oxidation stability at +1.23 V_{RHE} with j_{ph} maintained at or above 16 mA cm^2 (70% of initial j_{ph}). Such long stability was achieved by application of a UV filter and replacement of the catalyst-functionalized graphite sheet after 22 h (Fig. 4d).

These results allow the identification of four phases of IPV-anode degradation: a first burn-in phase in the first hour (more pronounced with UV light) is followed by a second, mostly linear j_{ph} decay related solely to the morphological instability of the photoactive layer as discussed above (Fig. 4c) and as demonstrated by the nearly perfect overlap of the j_{ph} decay profiles of the IPV-anode and an OPV with the same structure (Fig. 4d). Third, an accelerated photocurrent decay (after 22–26 h of continuous operation) is due to the loss of most of the NiFeOOH from the surface of the graphite sheet (Supplementary Fig. 27). Fourth, if the graphite sheet is not replaced or covered with a new one, the final phase occurs, which is the non-reversible, fast degradation (reportedly due to delamination of the otherwise photochemically stable organic materials)[14] by the aqueous electrolyte reaching the organic BHJ layer through the deteriorated graphite sheet (Supplementary Fig. 27).

The degradation of the graphite sheet was monitored by the water contact angle, which decreased from 86° to 55° over 72 h of continuous operation (Supplementary Fig. 34). In addition, scanning electron microscopy revealed significant morphological changes on the surface of the graphite, while the cross section remained unchanged (Supplementary Figs. 35 and 36). This catastrophic degradation was circumvented by repeated addition of a new graphite sheet upon signs of deterioration, which allowed demonstration of operational stability over 48 h (Supplementary Fig. 27). Alternatively, applying a combination of a denser (15% porosity) non-functionalized graphite sheet and a less dense (50% porosity) NiFeOOH-functionalized top graphite sheet allowed for 72 h long continuous water oxidation by the organic IPV-anodes and up to 100 h stability when replacing the graphite sheet twice (Supplementary Fig. 27). Recording the polarization curve of the IPV-anode before and after 72 h of solar water splitting reveals 38% reduction of j_{ph} at +1.23 V_{RHE} but only small change in the E_{on} (from +0.68 V_{RHE} to +0.62 V_{RHE}), further confirming that the operation of the IPV-anode in this case is mainly limited by the morphological instability of the organic BHJ layer (Supplementary Fig. 37). IPV-anodes containing polymer:polymer photoactive layers showed stability results comparable with the ternary PM6:D18:L8-BO devices, (Supplementary Fig. 38)

https://doi.org/10.1038/s41560-025-01736-6

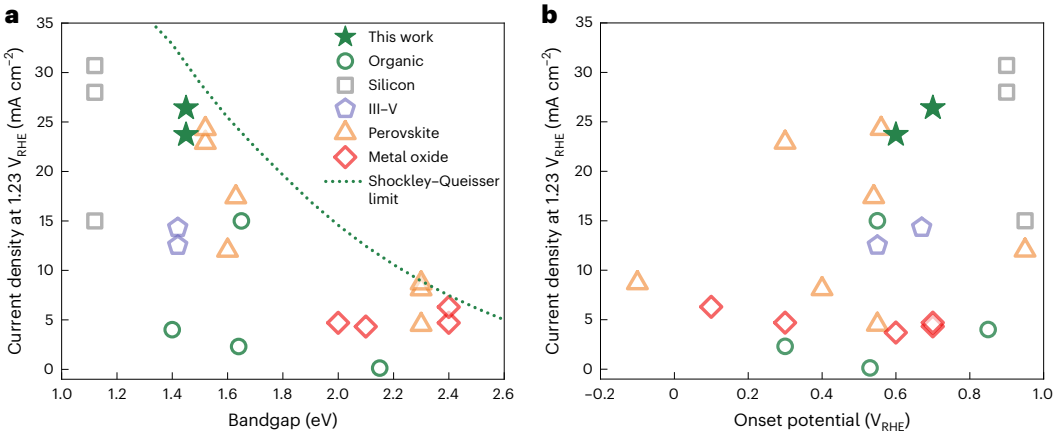

Fig. 5 | Performance comparison of a selection of reported single-junction fully integrated devices for solar water oxidation in PEC cells without any sacrificial agent. a,**b**, A comparison of reported photocurrent densities at +1.23 V_{RHE} as a function of the photoactive layer bandgap (**a**) and onset potential for linear rise of photocurrent (**b**). The Shockley–Queisser limit of photocurrent density with different semiconductor bandgaps is shown with a green dotted line. III–V, compound semiconductors containing elements from group III and group V of the periodic table.The performance parameters and composition of the compared devices are detailed in Supplementary Table 2 (refs. 14,16,17,22,37,38,43–57).

confirming the general applicability of the understanding gained on the degradation mechanism of these organic IPV-anodes.

Comparison with state-of-the-art photoanodes and IPV-anodes

Figure 5 displays a comparison of j_{ph} at +1.23 V_{RHE} reported for state-of-the-art fully integrated solar water oxidation devices (including both traditional photoanodes and IPV-anodes) without using any sacrificial agent. Most of the devices comprising organic semiconductors before this work generated a j_{ph} below 5 mA cm^{-2}, apart from one report demonstrating 15 mA cm^{-2} with an organic IPV-anode[14,16,17]. The highest j_{ph} of the PM6:D18:L8-BO and PM6:PY-IT devices presented in this Article (26.4 mA cm^{-2} and 23.7 mA cm^{-2}, respectively) mean a significant leap forward, showcasing the first organic IPV-anode with a j_{ph} above 25 mA cm^{-2}. Importantly, these high j_{ph} values are accompanied by days-long operational water oxidation stability in PEC cells, which is also a large improvement compared with previous organic photoanodes and IPV-anodes reporting stability of minutes or hours (Supplementary Table 2). Even when compared with IPV-anodes with different photoactive layers such as perovskites or silicon, the PM6:D18:L8-BO organic IPV-anode offers one of the highest j_{ph} so far for its given bandgap (Fig. 5a). The only reported IPV-anodes generating higher a j_{ph} are based on silicon photoactive layers, but these show a high E_{on} of +0.9 V_{RHE} or above due to their smaller 1.1 eV bandgap (Fig. 5b)[37,38].

Tandem organic IPV-anodes for unassisted operation

Finally, building on the developed single-junction PM6:D18:L8-BO devices, monolithic tandem IPV-anodes comprising two photoactive layers were fabricated and tested for unassisted (that is, bias-free) solar water splitting in conjunction with a platinum counter electrode (Fig. 6). The tandem cells comprise a wide-bandgap BHJ photoactive layer of GS-ISO, a non-fused non-fullerene acceptor, and PTQ10, a low synthetic complexity polymer donor with PM6:D18:L8-BO as the narrow-bandgap photo-absorber. The tandem IPV-anode shows a remarkably low E_{on} of −0.41 V_{RHE} in a three-electrode setup owing to its large photovoltage (Supplementary Fig. 39), which is also reflected in large ΔOCP value of 1.75 V (Supplementary Fig. 40). This allows for unassisted solar water splitting: the tandem IPV-anodes in a two-electrode setup demonstrated j_{ph} of 4.3 mA cm^{-2} at zero applied bias (Fig. 6a), which translates into 5% STH efficiency. The unassisted water splitting in the PEC cells was confirmed by the formation of O_2 bubbles on the tandem organic IPV-anode and H_2 bubbles on the counter electrode (Fig. 6b and Supplementary Video 1). The average Faradaic efficiency of the tandem IPV-anode in two-electrode, unassisted operation was 95% (Supplementary Fig. 41). Continuous operation at zero applied bias in two-electrode setup demonstrates the potential of the organic IPV-anodes for unassisted solar hydrogen generation (Fig. 6b). The application of a UV filter allowed 4 h unassisted solar water-splitting stability by the tandem device while maintaining 70% of the initial j_{ph} (Supplementary Fig. 42).

Comparing the tandem IPV-anode stabilities at applied biases of 0 V and tandem OPV stabilities at equivalent voltages of +1.8 V reveals that the j_{ph} in the IPV-anode is less stable under bias-free conditions partly due to the j_{ph} decay of the OPV. Accordingly, the tandem IPV-anodes demonstrate stable water oxidation at a high applied bias of +1.23 V_{RHE} in agreement with stable j_{ph} generated by the tandem OPV at 0 V (Supplementary Figs. 42 and 43). Interestingly, this degradation of the tandem IPV-anodes recovers after leaving them at OCP for a few hours (Supplementary Fig. 42). This recoverable degradation is partly attributed to the reversible morphological changes in the photoactive layers and is also probably influenced by the detachment of surface oxygen bubbles during the recovery period. Bubbles can alter the local pH and increase the overpotential for water oxidation, particularly when the IPV-anode is covered by large bubbles as shown in Fig. 6b and Supplementary Fig. 44 (refs. 39,40). More morphologically stable organic photoactive layers and management of bubbles will allow even longer unassisted solar water splitting by organic tandem IPV-anodes.

Conclusion

The presented fully integrated organic anodes with a BHJ PM6:D18:L8-BO photoactive layer demonstrate photocurrent densities above 25 mA cm^2 at +1.23 V_{RHE} and 40 h long operational solar water oxidation stability in PEC cells while maintaining 70% of the initial j_{ph}. Such high performance was achieved by the application of an inexpensive graphite sheet functionalized by the earth-abundant electrocatalyst NiFeOOH that served as a conductive, water-resistant top contact without introducing any electrical losses. This approach also allowed the fabrication of anodes integrating PM6:PY-IT polymer:polymer organic photoactive layer reaching photocurrent densities above 23 mA cm^2 at +1.23 V_{RHE} and a reduced onset potential of +0.63 V_{RHE}. Furthermore, monolithic tandem anodes integrating organic PM6:D18:L8-BO and PTQ10:GS-ISO photoactive layers were prepared reaching 5% STH efficiency in a two-electrode PEC setup, which highlights the potential of

https://doi.org/10.1038/s41560-025-01736-6

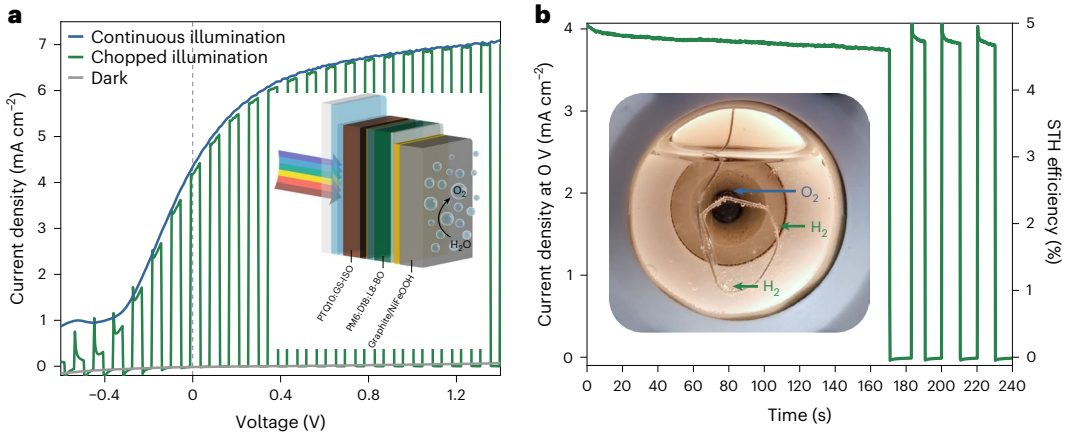

Fig. 6 | Performance of the monolithic organic tandem IPV-anode with PM6:D18:L8-BO and PTQ10:GS-ISO absorber layers in a two-electrode PEC cell. a, The current density–voltage scans at a 50 mV s^{-1} scan rate in dark, under 1 sun continuous and chopped illumination for the monolithic tandem IPV-anode in a two-electrode cell with a Pt counter electrode. The scan rate for the chopped illumination was 20 mV s^{-1}. The vertical dashed line indicates a zero applied potential. Inset: schematic structure of the monolithic organic tandem IPV-anode (not to scale). **b**, The unassisted, two-electrode operational PEC stability of the monolithic organic tandem under continuous (0–170 s) and chopped (170–240 s) 1 sun illumination. Inset: photograph of the tandem IPV-anode and counter electrode in unassisted operation generating O_2 and H_2 bubbles, respectively. The measurements were performed in a PEC cell with aqueous 1 M NaOH electrolyte.

integrating organic BHJ photoactive layers for stable, unassisted solar water splitting. A comparison of PEC and photovoltaic operations in terms of photocurrent stability and light-intensity-dependent performance, as well as PL measurements of the organic photoactive layer, suggest strategies for further improvement of the organic devices: the photostability of the active layer is a key factor to increase the overall operational stability and maintaining large quasi-Fermi level splitting (that is, illumination above 0.5 sun light intensity) in PEC operation is critical to avoid large recombination losses, while management of bubbles will allow more stable unassisted solar water splitting.

Methods

PM6:D18:L8-BO and PM6:PY-IT organic device fabrication

The ITO-coated glass substrates were cleaned sequentially in sonication baths of soapy water, water, acetone and isopropanol. Tin oxide (SnO_2) nanoparticle ink (Avantama N-31) was spin coated at 3,000 rpm onto the cleaned substrates and annealed at 200 °C for 30 min inside a glovebox. Poly((4,8-bis(5-(2-ethylhexyl)-4-fluoro-2-thienyl)benzo[1,2-*b*:4,5-*b*′]dithiophene-2,6-diyl)-2,5-thiophenediyl (5,7-bis(2-ethylhexyl)-4,8-dioxo-4*H*,8*H*-benzo[1,2-*c*:4,5-*c*′]dithiophene-1,3-diyl)-2,5-thiophenediyl)) (PM6), poly (dithieno[3,2-*e*:2′,3′-*g*]-2,-1,-3-benzothiadiazole-5,8-diyl(4-(2-butyloctyl)-2,5-thiophenediyl) (4,8-bis(5-(2-ethylhexyl)-4-fluoro-2-thienyl)benzo[1,2-*b*:4,5-*b*′] dithiophene-2, *6*-diyl) (3-(2-butyloctyl)-2,5-thiophenediyl)) (D18) and 2,2′-((2*Z*,2′*Z*)-((3,9-bis(2-butyloctyl)-12,13-bis(2-ethylhexyl)-12,13-dihydro-[1,2,5]thiadiazolo[3,4-*e*]thieno[2″,3″:4′,5′] thieno[2′,3′:4,5]pyrrolo[3,2-*g*]thieno[2′,3′:4,5] thieno[3,2-*b*] indole-2,10-diyl)bis(methaneylylidene))bis(5,6-difluoro-3-oxo-2,3-dihydro-1*H*-indene-2,1-diylidene))dimalononitrile (L8-BO), all from 1-Material, were dissolved at 14 mg ml^{-1} for thin devices or 20 mg ml^{-1} for thick devices in chloroform at weight ratios of 0.8:0.2:1.2, respectively, with 50% by total weight added diodobenzene and stirred for 2 h at 50 °C. The precursor solution was then spin coated at 3,000 rpm and annealed at 85 °C for 10 min on a hot plate to form the photoactive layers inside a glovebox. For PM6:PY-IT devices, PM6 and poly[(2,2′-((2*Z*,2′*Z*)-((12,13-bis(2-octyldodecyl)-3,9-diundecyl-12,13-dihydro[1,2,5]thiadiazolo[3,4-*e*]thieno[2″,3″:4′,5′] thieno[2′,3′:4,5] pyrrolo[3,2-*g*]thieno[2′,3′:4,5]thieno[3,2-*b*]-indole-2,10-diyl)bis(methanylylidene))bis(5-methyl-3-oxo -2,3-dihydro-1*H*-indene-2,1-diylidene))dimalononitrile-co-2,5-thiophene (PY-IT) from Solarmer were dissolved at a weight ratio of 1:1.2, respectively, at 18 mg ml^{-1} in chloroform, with 1% added chloronaphtalene, spin coated at 1,700 rpm for 30 s and annealed at 100 °C for 10 min. After PM6:D18:L8-BO or PM6:PY-IT deposition, subsequently 10 nm of MoO_3 and 30 nm of gold (for IPV-anodes) or 100 nm of silver (for solar cells) were evaporated on top of the active layers.

PTQ10:GS-ISO and PM6:D18:L8-BO tandem organic device fabrication

Poly[[6,7-difluoro[(2-hexyldecyl)oxy]-5,8-quinoxalinediyl]-2,5-thiophenediyl]]) (PTQ10) and GS-ISO[41] from 1-Material were dissolved overnight at 20 mg ml^{-1} in chloroform at a weight ratio of 1:1.5, respectively. The solution was spin cast at 3,000 rpm for 30 s onto ITO-coated glass/SnO_2 substrates and annealed at 145 °C for 25 min. Next, the samples were preheated at 120 °C, and BM-HTL-1 (Brilliant Matters), previously sonicated and filtered, was spin cast at 3,000 rpm for 50 s, followed by drying for 5 min at 100 °C. Subsequently, 1 nm of gold was evaporated; SnO_2 N-31 ink was spin cast at 3,000 rpm for 30 s and annealed at 145 °C for 10 min in a glovebox; and D18:PM6:L8-BO, MoO_3 and gold were deposited sequentially as described above.

Organic IPV-anode fabrication

The devices were protected for IPV-anode use by manually attaching on top of the thin metal electrode of the OPV one or more graphite sheet(s) with an acrylic adhesive layer on the back side and NiFeOOH on the top side. An 0.070-mm graphite sheet (self-adhesive, RS, Panasonic, 1,000 W m^{-1} K^{-1}, 115 mm × 90 mm) was applied and in some cases, a combination of a 0.025-mm-thick (self-adhesive, 1,600 W m^{-1} K^{-1}, 115 mm × 90 mm) and 0.150-mm-thick graphite sheets was used, as stated in figure captions (Fig. 4d and Supplementary Figs. 27, 33 and 42). The NiFeOOH was previously electrodeposited on the graphite sheet(s) using an aqueous solution of 40 mM of nickel sulfate hexahydrate (Sigma-Aldrich, ≥98%) and 10 mM of iron sulfate heptahydrate (Sigma-Aldrich, ≥99%), purged with N_2 for 30 min. A three-electrode setup with platinum counter electrode and a Ag/AgCl reference electrode was used for the electrodeposition. The potential was swept from +0.6 to +1.0 $V_{Ag/AgCl}$ at 20 mV s^{-1} scan rate until the electrodeposition charge density reached 4.2 mC cm^{-2}. For the control samples without the graphite sheet, NiFeOOH was electrodeposited on top of a 30- or 100-nm-thick Au layer directly, using the PEC cell. In these cases, the

electrolyte was changed in the cell, and the PEC characterization of the samples was performed immediately after electrodeposition. For the IPV-anodes with a Pt catalyst, the graphite sheets were functionalized by electrodeposition at constant −0.5 V in a three-electrode setup using the Ag/AgCl reference and Pt counter electrode, until the electrodeposition charge density reached 100 mC cm^{-2}.

Optoelectronic characterization

A Shimadzu UV-2600 spectrophotometer was used to obtain the UV–visible light spectra of the thin organic layers deposited on ITO-coated glass. Electroluminescence spectra were obtained using a 2450 Keithley source meter and a Shamrock 303 spectrograph and iDUS InGaAs array detector (Andor SR 303i-B, cooled to −90 °C). The bandgaps of individual materials and blends were calculated using the intersection between absorption and emission spectra.

The PL and Raman spectroscopy measurements on fresh and degraded devices were carried out at different sample positions using a Renishaw in Via Raman microscope with a 50× objective in backscattering configuration. A holographic notch filter was used to remove Rayleigh scattered light. A diffraction grating of 2400 l mm^{-1} was used for Raman measurements, and a grating of 300 l mm^{-1} was used for PL measurements. The laser spot (λ = 514 nm, $d \approx 10$ µm) was focused on to the photoactive layer through the glass substrate (through the back side of the sample with respect to the top, non-transparent graphite sheet side), and the power was adjusted to give an adequate signal while avoiding laser induced degradation; laser power was maintained between samples to allow comparison. During measurement, the samples were held in a Linkam stage under a flow of nitrogen to inhibit photooxidation.

(Photo)electrochemical and solar cell measurements

The (photo)electrodes were characterized in a three-electrode setup using an Ivium Compacstat potentiostat, platinum counter electrode, KCl-saturated Ag/AgCl reference electrode and an aqueous 1 M sodium hydroxide electrolyte, sometimes with the addition of Na_2SO_3 (0.2 M) and H_2O_2 (0.5 M). Lot Quantum Design xenon lamp was applied as illumination source with an AM 1.5 G filter and a circular mask with an area of 0.28 cm^2. A 1 sun (100 mW cm^{-2}) irradiance was calibrated by a certified International Light Technologies SEL623 photodetector. The equation $V_{RHE} = V_{Ag/AgCl} + 0.0592 \times pH + 0.1976$ was used to convert the potentials applied versus the Ag/AgCl reference electrode ($V_{Ag/AgCl}$) to applied potentials versus the reversible hydrogen electrode (V_{RHE}). The potential of the reference electrode ($V_{Ag/AgCl}$) was 0.1976 V versus the standard hydrogen electrode. The OCP of the photoelectrodes were measured under 1 sun illumination for 30 s, then in dark for another 30 s, and the difference when switching the light off was calculated to provide the value of ΔOCP. The current–voltage scans of the graphite sheets attached to glass substrates with and without the NiFeOOH catalyst were recorded with the same setup without illumination. Two-electrode (photo)electrochemical measurements of the tandem devices were performed with the same setup but with only a counter (platinum) and working electrode connection unless stated differently. Both the PEC and OPV devices were scanned from forward to reverse bias (reverse scan). The photoelectrodes were also characterized as solar cells using a Keithley 2400 source voltmeter and Newport Oriel solar simulator. The solar cell degradation was studied at ambient conditions with a 10 mV s^{-1} scan rate.

The operational PEC photocurrent stability of IPV-anodes was measured under continuous 1 sun illumination, at an applied bias of +1.23 V_{RHE} for three-electrode measurements. Pyroscience FireStingO2 fibre-optic oxygen meter with a TROXROB10 oxygen probe and a TDIP temperature sensor was used to measure the percentage of oxygen (P_{O2}) in the defined overhead volume (V). After correcting for the dark baseline, the measured amount of oxygen ($n_{O2,m}$) generated by the IPV-anode under 1 sun illumination was calculated ($n_{O2} = n \times P_{O2}$) based on the measured pressure (p) and temperature (T) using the ideal gas law. A gas-tight cell was used, which was purged with nitrogen before the measurement. The amount of dissolved oxygen in the electrolyte was calculated applying Henry's law and added to the amount measured in the overhead space. The theoretical amount of oxygen ($n_{O2,t}$) was calculated for every second of the measurement from the measured photocurrent based on the equation $Q = n_{e^-} \times F$, where Q is the number of charges (C), n_{e^-} is the number of electrons (mol) and F is the Faraday constant (96,485.3 C mol^{-1}). The generation of 1 mol oxygen was considered to involve 4 mol of electrons. From the measured amount of oxygen and the theoretical amount of oxygen based on the measured photocurrent, the Faradaic efficiency (FE) was calculated ($FE = n_{O2,m}/n_{O2,t}$) for every second of the measurement. The onset of the measured P_{O2} was shifted in time to overlap with the measured photocurrent. The final value of the FE was calculated by averaging the FE values for the full plotted time of the measurement (1,200 s for the single-junction and 3,600 s for the tandem IPV-anodes). MSH-300F LOT Quantum Design monochromator was used to record the photocurrents generated under selected wavelength illumination and calculate IPCE. The intensity of the monochromatic light was measured using a certified International Light Technologies SEL033/U photodetector, which allowed us to obtain IPCE spectra in the 300–1,000 nm range. The STH efficiency of the tandem IPV-anode was calculated from the photocurrent density measured in the two-electrode setup, under 1 sun illumination without any applied bias (j_{sc}) using the following formula: $STH = |j_{sc}| \times (1.23\ V) \times FE/100\ mW\ cm^{-2}$.

Energy level measurements

The cube root photoemission of the samples was measured by ambient photoemission spectroscopy (APS, KP Technology, SKP5050) and extrapolated to zero, to determine the valence band edge, E_v, values of the thin layers. Monochromatic UV light irradiation was scanned in the 4.4–6.4 eV range. Kelvin probe measurements were used to record contact potential difference between the tip and the sample. A cleaned silver reference was used to calibrate the tip work function, which then allowed us to determine the Fermi level of the samples taking into account the measured contact potential difference of the samples and the work function of the tip. The E_v and conduction band edge, E_c, values of SnO_2 were not measured; instead, the E_c was estimated 0.2 eV above the measured E_F, which is typical for strong n-type materials[32,42].

Characterization of degraded samples

A Thermo Fisher K-Alpha+ X-ray photoelectron spectrometer with monochromated, micro-focused Al K_α X-ray source was used to obtain the XPS spectra of the fresh and degraded catalytic graphite sheets. All binding energies of all spectra were corrected using the 284.8 eV adventitious carbon peak as reference. The water contact angle of the graphite sheets was measured by a Kruss drop shape analyser (DSA25B). The contact angle was determined using the Young–Laplace method.

Reporting summary

Further information on research design is available in the Nature Portfolio Reporting Summary linked to this article.

Data availability

All data generated or analysed during this study are included in the Article and its Supplementary Information. Source data are provided with this paper. These data are also available via Figshare at https://doi.org/10.6084/m9.figshare.28169375 (ref. 58).

References

1. Lewis, N. S. & Nocera, D. G. Powering the planet: chemical challenges in solar energy utilization. *Proc. Natl Acad. Sci. USA* **103**, 15729–15735 (2006).

2. Pinaud, B. A. et al. Technical and economic feasibility of centralized facilities for solar hydrogen production via photocatalysis and photoelectrochemistry. *Energy Environ. Sci.* **6**, 1983–2002 (2013).
3. Shaner, M. R., Atwater, H. A., Lewis, N. S. & McFarland, E. W. A comparative technoeconomic analysis of renewable hydrogen production using solar energy. *Energy Environ. Sci.* **9**, 2354–2371 (2016).
4. van der Spek, M. et al. Perspective on the hydrogen economy as a pathway to reach net-zero CO_2 emissions in Europe. *Energy Environ. Sci.* **15**, 1034–1077 (2022).
5. Schneidewind, J. & Schneidewind, J. How much technological progress is needed to make solar hydrogen cost-competitive? *Adv. Energy Mater.* **12**, 2200342 (2022).
6. Moss, B., Babacan, O., Kafizas, A. & Hankin, A. A review of inorganic photoelectrode developments and reactor scale-up challenges for solar hydrogen production. *Adv. Energy Mater.* **11**, 2003286 (2021).
7. Zhang, G. et al. Renewed prospects for organic photovoltaics. *Chem. Rev.* **122**, 14180–14274 (2022).
8. Espinosa, N., Hösel, M., Angmo, D. & Krebs, F. C. Solar cells with one-day energy payback for the factories of the future. *Energy Environ. Sci.* **5**, 5117–5132 (2012).
9. Zhu, L. et al. Single-junction organic solar cells with over 19% efficiency enabled by a refined double-fibril network morphology. *Nat. Mater.* **21**, 656–663 (2022).
10. Cho, H. H. & Sivula, K. Advancing operational stability and performance of organic photoanodes for solar water oxidation. *Trends Chem.* **4**, 93–95 (2022).
11. Yao, L. et al. Organic semiconductor based devices for solar water splitting. *Adv. Energy Mater.* **8**, 1802585 (2018).
12. Steier, L. & Holliday, S. A bright outlook on organic photoelectrochemical cells for water splitting. *J. Mater. Chem. A* **6**, 21809–21826 (2018).
13. Zhang, D. et al. An organic semiconductor photoelectrochemical tandem cell for solar water splitting. *Adv. Energy Mater.* **12**, 2202363 (2022).
14. Cho, H. H. et al. A semiconducting polymer bulk heterojunction photoanode for solar water oxidation. *Nat. Catal.* **4**, 431–438 (2021).
15. Yao, L. et al. Establishing stability in organic semiconductor photocathodes for solar hydrogen production. *J. Am. Chem. Soc.* **142**, 7795–7802 (2020).
16. Ho Lee, T. et al. A dual functional polymer interlayer enables near-infrared absorbing organic photoanodes for solar water oxidation. *Adv. Energy Mater.* **12**, 2103698 (2022).
17. Yu, J. M. et al. High-performance and stable photoelectrochemical water splitting cell with organic-photoactive-layer-based photoanode. *Nat.Commun.* **11**, 5509 (2020).
18. Thangamuthu, M. et al. Polymer photoelectrodes for solar fuel production: progress and challenges. *Chem. Rev.* **122**, 11778–11829 (2022).
19. Kirner, J. T. & Finke, R. G. Water-oxidation photoanodes using organic light-harvesting materials: a review. *J. Mater. Chem. A* **5**, 19560–19592 (2017).
20. Wang, L. et al. Improved stability and performance of visible photoelectrochemical water splitting on solution-processed organic semiconductor thin films by ultrathin metal oxide passivation. *Chem. Mater.* **30**, 324–335 (2018).
21. Steier, L. et al. Stabilizing organic photocathodes by low-temperature atomic layer deposition of TiO_2. *Sustain. Energy Fuels* **1**, 1915–1920 (2017).
22. Daboczi, M. et al. Scalable all-inorganic halide perovskite photoanodes with >100 h operational stability containing earth-abundant materials. *Adv. Mater.* **35**, 2304350 (2023).
23. Fehr, A. M. K. et al. Integrated halide perovskite photoelectrochemical cells with solar-driven water-splitting efficiency of 20.8. *Nat. Commun.* **14**, 3797 (2023).
24. Rühle, S. Tabulated values of the Shockley–Queisser limit for single junction solar cells. *Sol. Energy* **130**, 139–147 (2016).
25. Yue, Y. et al. All-polymer solar cells with 17% efficiency enabled by the 'end-capped' Ternary strategy. *Adv. Sci.* **9**, 2204030 (2022).
26. Formal Le, F., Grätzel, M. & Sivula, K. Controlling photoactivity in ultrathin hematite films for solar water-splitting. *Adv. Funct. Mater.* **20**, 1099–1107 (2010).
27. Street, R. A., Krakaris, A. & Cowan, S. R. Recombination through different types of localized states in organic solar cells. *Adv. Funct. Mater.* **22**, 4608–4619 (2012).
28. Ma, L. K. et al. High-efficiency indoor organic photovoltaics with a band-aligned interlayer. *Joule* **4**, 1486–1500 (2020).
29. Du, C. et al. Hematite-based water splitting with low turn-on voltages. *Angew. Chem. Int. Ed.* **52**, 12692–12695 (2013).
30. Power, G. P. & Ritchie, I. M. Mixed potentials: experimental illustrations of an important concept in practical electrochemistry. *J. Chem. Educ.* **60**, 1022–1026 (1983).
31. Bai, Y. et al. Interfacial engineering and optical coupling for multicolored semitransparent inverted organic photovoltaics with a record efficiency of over 12%. *J. Mater. Chem. A* **7**, 15887–15894 (2019).
32. Luke, J. et al. A commercial benchmark: light-soaking free, fully scalable, large-area organic solar cells for low-light applications. *Adv. Energy Mater.* **11**, 2003405 (2021).
33. Di Mario, L. et al. Outstanding fill factor in inverted organic solar cells with SnO_2 by atomic layer deposition. *Adv. Mater.* **36**, 2301404 (2023).
34. Luke, J. et al. Strong intermolecular interactions induced by high quadrupole moments enable excellent photostability of non-fullerene acceptors for organic photovoltaics. *Adv. Energy Mater.* **12**, 2201267 (2022).
35. Razzell-Hollis, J., Limbu, S. & Kim, J. S. Spectroscopic investigations of three-phase morphology evolution in polymer: fullerene solar cell blends. *J. Phys. Chem. C* **120**, 10806–10814 (2016).
36. Wang, Y. et al. The critical role of the donor polymer in the stability of high-performance non-fullerene acceptor organic solar cells. *Joule* **7**, 810–829 (2023).
37. Zhou, X. et al. Interface engineering of the photoelectrochemical performance of Ni-oxide-coated *n*-Si photoanodes by atomic-layer deposition of ultrathin films of cobalt oxide. *Energy Environ. Sci.* **8**, 2644–2649 (2015).
38. Yu, X. et al. NiFe alloy protected silicon photoanode for efficient water splitting. *Adv. Energy Mater.* **7**, 1601805 (2017).
39. Mavrič, A. & Cui, C. Advances and challenges in industrial-scale water oxidation on layered double hydroxides. *ACS Appl. Energy Mater.* **4**, 12032–12055 (2021).
40. Cheng, X. et al. Bubble management for electrolytic water splitting by surface engineering: a review. *Langmuir* **39**, 16994–17008 (2023).
41. Bi, P. et al. A high-performance nonfused wide-bandgap acceptor for versatile photovoltaic applications. *Adv. Mater.* **34**, 2108090 (2022).
42. Martínez-Puente, M. A. et al. Unintentional hydrogen incorporation into the SnO_2 electron transport layer by ALD and its effect on the electronic band structure. *ACS Appl. Energy Mater.* **4**, 10896–10908 (2021).
43. Liu, G., Chen, C., Ji, H., Ma, W. & Zhao, J. Photoelectrochemical water splitting system with three-layer n-type organic semiconductor film as photoanode under visible irradiation. *Sci. China Chem.* **55**, 1953–1958 (2012).

44. Wang, S. et al. Synergistic crystal facet engineering and structural control of WO_3 films exhibiting unprecedented photoelectrochemical performance. *Nano Energy* **24**, 94–102 (2016).
45. Kim, J. Y. et al. Single-crystalline, wormlike hematite photoanodes for efficient solar water splitting. *Sci. Rep.* **3**, 2681 (2013).
46. Peerakiatkhajohn, P. et al. Stable hematite nanosheet photoanodes for enhanced photoelectrochemical water splitting. *Adv. Mater.* **28**, 6405–6410 (2016).
47. Cui, J. et al. 2D bismuthene as a functional interlayer between $BiVO_4$ and NiFeOOH for enhanced oxygen-evolution photoanodes. *Adv. Funct. Mater.* **32**, 2207136 (2022).
48. He, B. et al. General and robust photothermal-heating-enabled high-efficiency photoelectrochemical water splitting. *Adv. Mater.* **33**, 2004406 (2021).
49. Poli, I. et al. Graphite-protected $CsPbBr_3$ perovskite photoanodes functionalised with water oxidation catalyst for oxygen evolution in water. *Nat. Commun.* **10**, 2097 (2019).
50. Yang, H. et al. Monolithic $FAPbBr_3$ photoanode for photoelectrochemical water oxidation with low onset-potential and enhanced stability. *Nat. Commun.* **14**, 5486 (2023).
51. Tao, R., Sun, Z., Li, F., Fang, W. & Xu, L. Achieving organic metal halide perovskite into a conventional photoelectrode: outstanding stability in aqueous solution and high-efficient photoelectrochemical water splitting. *ACS Appl. Energy Mater.* **2**, 1969–1976 (2019).
52. Wang, M. et al. High-performance and stable perovskite-based photoanode encapsulated by blanket-cover method. *ACS Appl. Energy Mater.* **4**, 7526–7534 (2021).
53. Choi, H. et al. Suppression of undesired losses in organometal halide perovskite-based photoanodes for efficient photoelectrochemical water splitting. *Adv. Energy Mater.* **13**, 2300951 (2023).
54. Kim, T. G. et al. Monolithic lead halide perovskite photoelectrochemical cell with 9.16% applied bias photon-to-current efficiency. *ACS Energy Lett.* **7**, 320–327 (2022).
55. Chen, Y. W. et al. Atomic layer-deposited tunnel oxide stabilizes silicon photoanodes for water oxidation. *Nat. Mater.* **10**, 539–544 (2011).
56. Hu, S. et al. Amorphous TiO_2 coatings stabilize Si, GaAs, and GaP photoanodes for efficient water oxidation. *Science* **344**, 1005–1009 (2014).
57. Kang, D. et al. Printed assemblies of GaAs photoelectrodes with decoupled optical and reactive interfaces for unassisted solar water splitting. *Nat. Energy* **2**, 17043 (2017).
58. Daboczi, M. et al. Dataset for 'Enhanced solar water oxidation and unassisted water splitting using graphite protected bulk heterojunction organic photoactive layers' *figshare* https://doi.org/10.6084/m9.figshare.28169375 (2025).

Acknowledgements

M.D. and S.E. acknowledge the funding of UK Engineering and Physical Sciences Research Council provided via grant no. EP/S030727/1. F.E. and J.N. acknowledge financial support from the European Research Council (action no. 742708). M.D. acknowledges support received from Imperial College London, Postdoc and Fellows Development Centre Fund—Seeds for Success (2022) and from the European Union under the Marie Skłodowska-Curie Actions grant agreement no. 101103762. F.E. acknowledges support through the Imperial College Research Fellowship. J.L. and J.-S.K. acknowledge the UK Engineering and Physical Sciences Research Council for the ATIP Programme grant (grant no. EP/T028513/1).

Author contributions

M.D., F.E., J.N. and S.E. conceived, designed and supervised the project. F.E., S.W.Y., N.A.L. and M.Z. fabricated the photoelectrodes, while M.D. performed the PEC experiments. M.Y. helped with performing XPS measurements. J.L., K.S. and J.-S.K. aided with the characterization by Raman spectroscopy. N.A.L. performed the UV–visible light spectroscopy. J.S.M. performed the energy level, electroluminescence, light-intensity-dependent current–voltage and external quantum efficiency measurements. M.D. and F.E. wrote the paper with the support of J.L., J.N. and S.E. All authors contributed to analysing and discussing the results.

Competing interests

The authors declare no competing interests.

Additional information

Supplementary information The online version contains supplementary material available at https://doi.org/10.1038/s41560-025-01736-6.

Correspondence and requests for materials should be addressed to Matyas Daboczi, Flurin Eisner, Jenny Nelson or Salvador Eslava.

Peer review information *Nature Energy* thanks Néstor Guijarro and the other, anonymous, reviewer(s) for their contribution to the peer review of this work.

nature research

Corresponding author(s): Dr Salvador Eslava

Solar Cells Reporting Summary

Nature Research wishes to improve the reproducibility of the work that we publish. This form is intended for publication with all accepted papers reporting the characterization of photovoltaic devices and provides structure for consistency and transparency in reporting. Some list items might not apply to an individual manuscript, but all fields must be completed for clarity.

For further information on Nature Research policies, including our data availability policy, see Authors & Referees.

Experimental design

Please check: are the following details reported in the manuscript?

1. Dimensions

Area of the tested solar cells	☒ Yes ☐ No	The information can be found in the figure captions as well as in the "(Photo)electrochemical and solar cell measurements" section in Methods.
Method used to determine the device area	☒ Yes ☐ No	The information can be found in "(Photo)electrochemical and solar cell measurements" section in Methods. Circular mask with predefined diameters was used: "...a circular mask with an area of 0.28 cm2."

2. Current-voltage characterization

Current density-voltage (J-V) plots in both forward and backward direction	☐ Yes ☒ No	The hysteresis for organic solar cells is mostly negligible and usually not measured.
Voltage scan conditions *For instance: scan direction, speed, dwell times*	☒ Yes ☐ No	The scan rate used for the photoelectrochemical as well as solar measurements is stated in each figure caption separately. The rest of the information can be found in "(Photo)electrochemical and solar cell measurements" section in Methods.
Test environment *For instance: characterization temperature, in air or in glove box*	☒ Yes ☐ No	The environment (typically ambient, aqueous 1 M NaOH electrolyte) is stated in each figure caption separately, as well as in the "(Photo)electrochemical and solar cell measurements" section in Methods.
Protocol for preconditioning of the device before its characterization	☐ Yes ☒ No	The devices were not preconditioned before characterization.
Stability of the J-V characteristic *Verified with time evolution of the maximum power point or with the photocurrent at maximum power point; see ref. 7 for details.*	☒ Yes ☐ No	Information on the operational stability tests of the photoelectrodes can be found in the figure captions (e.g., Fig. 4) and in "(Photo)electrochemical and solar cell measurements" section in Methods.

3. Hysteresis or any other unusual behaviour

Description of the unusual behaviour observed during the characterization	☐ Yes ☒ No	Not applicable.
Related experimental data	☐ Yes ☒ No	Not applicable.

4. Efficiency

External quantum efficiency (EQE) or incident photons to current efficiency (IPCE)	☒ Yes ☐ No	IPCE spectrum of the highest performing photoelectrode is shown in Fig. 2e. Details of the measurement are provided in the "(Photo)electrochemical and solar cell measurements" section in Methods.
A comparison between the integrated response under the standard reference spectrum and the response measure under the simulator	☒ Yes ☐ No	The integrated photocurrent density under 1 sun illumination is reported in Fig. 2e, while the photocurrent densities of the photoelectrodes under 1 sun illumination are displayed in Fig. 2a and Fig 2b.
For tandem solar cells, the bias illumination and bias voltage used for each subcell	☒ Yes ☐ No	Only monolithic tandem photoelectrodes were measured, meaning that the applied bias and illumination was always the same for the subcells. The conditions of the measurements are detailed in the figure captions (e.g., Fig. 6).

5. Calibration

Light source and reference cell or sensor used for the characterization	☒ Yes ☐ No	The information can be found in "(Photo)electrochemical and solar cell measurements" section in Methods.

Confirmation that the reference cell was calibrated and certified	☒ Yes ☐ No	The information can be found in "(Photo)electrochemical and solar cell measurements" section in Methods: "Lot Quantum Design xenon lamp was applied as illumination source with an AM 1.5G filter and a circular mask with an area of 0.28 cm2. 1 sun (100 mW cm-2) irradiance was calibrated by a certified International Light Technologies SEL623 photodetector"
Calculation of spectral mismatch between the reference cell and the devices under test	☐ Yes ☒ No	Minimal spectral mismatch was confirmed by comparing the integrated photocurrent density under 1 sun illumination (reported in Fig. 2e and the photocurrent densities of the photoelectrodes under 1 sun illumination (displayed in Fig. 2a). Further information can be found in "(Photo)electrochemical and solar cell measurements" section in Methods.

6. Mask/aperture

Size of the mask/aperture used during testing	☒ Yes ☐ No	The information can be found in "(Photo)electrochemical and solar cell measurements" section in Methods. Circular mask with predefined diameters was used: "...a circular mask with an area of 0.28 cm2."
Variation of the measured short-circuit current density with the mask/aperture area	☒ Yes ☐ No	The influence of device active area is discussed in the manuscript in the "PEC performance of organic photoanodes" section.

7. Performance certification

Identity of the independent certification laboratory that confirmed the photovoltaic performance	☐ Yes ☒ No	The focus of the work is the photoelectrode performance and so the photovoltaic performance was not certified by an independent certification laboratory.
A copy of any certificate(s) *Provide in Supplementary Information*	☐ Yes ☒ No	The focus of the work is the photoelectrode performance and so the photovoltaic performance was not certified by an independent certification laboratory.

8. Statistics

Number of solar cells tested	☒ Yes ☐ No	Supplementary Fig. 13 shows current-voltage curves of 7 organic photoelectrodes from different batches prepared by the same method. Supplementary Fig. 11 shows current-voltage curves of 10 organic solar cells from different batches prepared by the same method.
Statistical analysis of the device performance	☒ Yes ☐ No	Statistical analysis of photoelectrode performance is provided in Fig. 2 b, while statistical analysis of the organic solar cell performance is shown in Supplementary Fig. 11.

9. Long-term stability analysis

Type of analysis, bias conditions and environmental conditions *For instance: illumination type, temperature, atmosphere humidity, encapsulation method, preconditioning temperature*	☒ Yes ☐ No	Information on the operational stability tests of the photoelectrodes can be found in the figure captions and in the "(Photo)electrochemical and solar cell measurements" section in Methods.